UC Davis
UC Davis Previously Published Works

Title
Tomographic imaging with Compton PET modules: ideal case and first implementation

Permalink
https://escholarship.org/uc/item/2fq9c34q

Journal
Journal of Instrumentation, 16(04)

ISSN
1748-0221

Authors
Peng, P
Zhang, M
Zeraatkar, N
et al.

Publication Date
2021-04-01

DOI
10.1088/1748-0221/16/04/t04007

Peer reviewed

eScholarship.org Powered by the California Digital Library
University of California

Author Manuscript
Author Manuscript
Author Manuscript
Author Manuscript

HHS Public Access
Author manuscript
J Instrum. Author manuscript; available in PMC 2022 April 01.

Published in final edited form as:
J Instrum. 2021 April ; 16(4): . doi:10.1088/1748-0221/16/04/t04007.

Tomographic imaging with Compton PET modules: ideal case and first implementation

P. Peng[a,*], **M. Zhang**[a], **N. Zeraatkar**[a], **J. Qi**[a], **S.R. Cherry**[a]

[a]Department of Biomedical Engineering, University of California-Davis One Shields Avenue, Davis, CA 95616, USA

Abstract

In our previous studies, we demonstrated that the Compton PET module, a layer structure PET detector with side readout, can provide high performance in terms of spatial/energy/timing resolution, as well as high gamma ray detection efficiency. In this study, we investigate how to translate the high performance of the detector module into good quality reconstructed tomographic images. This study is performed using GATE simulation, as well as with physical experiments. Similar detector geometry is used in the simulation and experiment: two identical 4-layer detector modules are placed with face to face distance of 56 mm. In the simulation study, each layer consists of a 1-mm-pitch pixelated crystal array. In the experimental study, each layer is a monolithic crystal, which is virtually binned into 1 mm^2 cells to group single events according to the gamma ray interaction locations. A customized Derenzo phantom was placed between the two detector modules. By rotating the phantom using a motorized rotary stage, data along lines of response (LORs) at different angles were collected for reconstructing the tomographic image. The same reconstruction algorithm was used for both simulation and experimental studies. The results demonstrate that the simulation study could resolve 0.8 mm rods while the experimental study was able to resolve 1.0 mm rods.

Keywords

Compton PET; Monte Carlo; GATE; Derenzo phantom; Reconstruction

1. Introduction

Positron emission tomography (PET) is the most sensitive non-invasive imaging modality to study radiotracer distribution in human subjects in vivo [1]. However, due to a PET scanner's small solid angle coverage and limited gamma ray detection efficiency, only a small portion (~1%) of the coincidence photon pairs emitted from the scanned subject are typically recorded. This inefficient detection of the emitted gamma photons limits the spatial-temporal resolution that a PET scanner can achieve. One way to increase the scanner's sensitivity is to increase its solid angle coverage. As in the case of uEXPLORER total-body PET/CT scanner, the sensitivity has been increased by 40-fold for total-body imaging due to its 194 cm axial length [2]. On the other hand, using a thicker scintillator can

* pppeng@ucdavis.edu .

Author Manuscript Author Manuscript Author Manuscript Author Manuscript

also increase a scanner's sensitivity because of its higher gamma ray detection efficiency. However, for conventional detector designs with pixelated crystal array, thicker scintillators will degrade the scanner's energy and timing resolution, due to a decrease in light collection efficiency as the crystal becomes longer [3]. Moreover, thicker scintillator will lead to worse parallax errors if the detectors provide no depth of interaction (DOI) information [4]. For monolithic detector designs, the spatial resolution degrades with increasing scintillator thickness [5, 6]. To mitigate these negative effects on detector performance when using thicker scintillator, a layer structure detector design with side readout has recently been proposed [7–11]. In this side readout design, even though scintillation light needs to be detected on all four sides of the module, it is possible to use fewer photodetectors than a conventional detector design by using a detector module with relatively large cross-sectional area compared to its depth, or using sparsely populated photodetectors [9]. A detector characterization study has shown that the scintillator thickness can be increased without affecting the detector performance in terms of spatial/energy/timing resolution [12]. The higher detector sensitivity allows the scanner to collect the same statistics at the same spatial resolution in a shorter time frame, thus increases the scanner's spatiotemporal resolution. High-spatiotemporal-resolution PET scanners will in turn open up more research and clinical applications related to tracer dynamic processes inside human body [13]. In this study, to verify the benefits of the layer structure detector, we moved from detector measurements to imaging studies by collecting data from a customized Derenzo phantom using a scanner composed of two Compton PET modules. The phantom is placed on a rotating stage allowing lines of response (LORs) at all possible angles to be collected for image reconstruction. We performed this study both with GATE (Geant4 Application for Tomographic Emission) Monte Carlo simulation [14] and experimentally to evaluate current and theoretical performance of this approach.

2. Material and methods

2.1 Structure of the detector module

Both the detector modules used in simulation and in experiment have 4 layers as shown in Figure 1. For ease of implementation, and to utilize previously validated code, in the simulated detector (Figure 1a), each layer is subdivided into a 13×13 pixelated array of LYSO crystals. The cross-sectional area of the array is 13×13 mm^2. Each crystal in the array has dimensions of 1×1×2.76 mm^3. There is no gap or reflector between crystals in the array of each layer. Therefore, there are no optical boundaries and a packing fraction of 100% within each layer thus simulating an actual monolithic crystal. Note that although there is a 0.6-mm reflector between adjacent layers in the experimental detectors, the reflectors are not simulated and are modelled only by air gaps of 0.6 mm (see Figure 1a). In the experimental detector (Figure 1b), each layer is a monolithic LYSO crystal slab (Crystal Photonics Inc., Sanford, FL) with dimensions of 13.34×13.34×2.76 mm^3. Three enhanced spectral reflective (ESR) films (Vikuiti™, 3M, St. Paul, MN) with a thickness of 0.6 mm are inserted between adjacent layers. Two more ESR films are used to cover the top and bottom surfaces of the module as well. These ESR films are not shown in Figure 1b.

Author Manuscript Author Manuscript Author Manuscript Author Manuscript

The specifications of this detector module with more details was previously described [12]. In the experiments, the gamma ray interaction position is estimated using the scintillation light intensity measured by the SiPMs (SensL ArrayJ-30035-16P) on the four sides of the crystal utilizing a machine learning approach [9, 10]. Based on the interaction positions, all the events are binned into 13×13 virtual pixels denoted by the white lines in Figure 1b. The pitch between neighbouring virtual pixels is 1 mm. Therefore, in this way, the intrinsic spatial resolution for the experimental detector (Figure 1b) is almost the same as the simulated detector (Figure 1a). However, the cross-sectional area of the monolithic crystal is 13.34×13.34 mm^2, thus, the virtual pixel size near the edges are larger than 1 mm^2 i.e., 1.17×1 mm^2 for edge pixels and 1.17×1.17 mm^2 for corner pixels. This difference will make the intrinsic spatial resolution of the experimental detector slightly worse than that of the simulated detector in the edge and corner regions.

2.2 Simulation Setup

We performed two sets of simulations in this study using GATE. In the first simulation, we used one pair of detector modules placed facing each other. We then made the two modules rotate around the scanner's axial center to collect LORs with sufficient angles to reconstruct a tomographic image (Figure 2). This was similar to our experiment setup for comparison. In the second simulation, we modeled a full-ring scanner with 12 detector modules (Figure 3). The purpose of the second simulation was to study the scenario if a complete scanner was assembled.

2.2.1 2-module scanner simulation—We simulated the 2-module system in GATE as shown in Figure 2, with a face to face distance between the two modules of 56 mm. Each detector module had the same geometry as in Figure 1a. We used the "OPET" system, which was one of the pre-defined systems in GATE. A customized Derenzo phantom was used as the radiation source with four segments with the following rod diameters: 0.8, 1.0, 1.4, and 1.8 mm. The distances between adjacent rods in each segment were twice their diameters. The phantom was a cylinder of 3.2 mm length and was geometrically centered in the scanner for acquisition. The emission was modeled by back-to-back 511-keV gamma rays. The rods activity concentration was set to ~25 kBq/mm^3. No scattering or attenuating medium was simulated. We simulated two different angular steps of 30° and 7.5°, as shown in Figure 2 (a) and (b), for rotating the detector module pair around the phantom. These two angular steps were simulated to investigate the effect of LOR sampling on the reconstructed image. There were 6 and 24 rotation positions for the two cases above, respectively, to cover all the angular positions in the transverse plane. The data acquisition time simulated for each position in the 30° and 7.5° cases was 450 and 112 seconds, respectively. These two simulations therefore collected a similar total number of coincidence events: ~7.8 million trues. Moreover, energy resolution, energy window, coincidence window, and delay window were set to 10%, 425–650 keV, 2.7 ns, and 200 ns, respectively, in the simulation.

2.2.2 Full-ring scanner simulation—The simulated full-ring scanner (Figure 3) had 12 detector modules with gantry inner diameter of 56 mm. Each detector module had the same geometry as explained in section 2.1 and shown in Figure 1a. The simulation of a 380-second data acquisition resulted in ~7.8 million true events. Since in the full-ring case,

Author Manuscript Author Manuscript Author Manuscript Author Manuscript

the true events could come from LORs connecting two modules not necessarily in opposite positions, the time to acquire similar number of true events for the full-ring case (i.e., 380 seconds) was shorter than the one for each position in the 30° case (i.e., 450 seconds).

2.3 Experimental Setup

We built two Compton PET modules (Figure 1b) for performing the tomographic imaging study experimentally. The two modules were placed face to face with a customized Derenzo phantom in the middle (Figure 4a). The distance between the front faces of the detector modules was 56 mm. The 3D printed Derenzo phantom (Figure 4b) was mounted on a rotary stage to allow us to collect coincidence events at the desired angles.

As in the simulation study, the phantom had 4 segments with rod diameters of 0.8, 1.0, 1.4, and 1.8 mm. The distances between adjacent rods in each segment were twice their diameters. The rods were hollow cylinders with axial length of 3.2 mm and were filled with [F-18]-fluorodeoxyglucose (FDG) with an activity concentration of ~37 kBq/mm^3 at the beginning of the measurement. Figure 4c schematically shows how the detector modules were connected to the data acquisition system (PETsys TOFPET-2 evaluation kit, Oeiras, Portugal). Although the system in this setup is capable of collecting both singles and coincidences, in this experiment we only stored the coincidence events. During the experiment, the motorized rotary stage rotated the phantom with an angular step of 7.5°, the same as the simulation study as shown in Figure 2b. Data was acquired at each position for 10 seconds, with 8 complete revolutions of the phantom (48 angles per revolution, 384 positions in total). This procedure allowed acquisition of similar number of coincidence events for each relative detector-phantom position as the source decayed. In total, we collected ~7.7 million prompt events.

2.4 Reconstruction Algorithm

We used the same reconstruction algorithm for both the simulation and the experimental studies: 160 iterations of the MLEM algorithm [15]. The images were reconstructed using 77 × 77 × 13 voxels with a voxel size of 0.5 × 0.5 × 1 mm^3 resulting in a reconstructed field of view (FOV) of 37.5 × 37.5 × 13 mm^3. The multi-layer structure of the detector module allowed us to identify a Compton scattering event if energy was collected in more than one layer, from which the first interaction location between the gamma ray and the crystal could be estimated. In this work, we only considered single-layer events for the experimental study; for the simulation study, all events were considered, in which the layer information was determined by the weighted mean method in GATE. The benefit of using the Compton scatter information on image quality will be studied in the future. In the simulation studies, only true events were used for reconstruction, thus no scatter or random correction was needed; in the experimental study, the prompt events (true + scatter + random) were used in the reconstruction, and neither scatter or random correction was performed. Geometric correction was performed for both simulation and experimental data using the sensitivity map calculated based on the LOR sampling in each scan geometry (Figure 5). No normalization for detector efficiency was performed. No point spread function (PSF) modeling or attenuation correction (AC) was used for reconstruction. The detector modules used in this study had a timing resolution of 348 ps [12], which

Author Manuscript Author Manuscript Author Manuscript Author Manuscript

corresponds to a spatial FWHM of the TOF kernel of 5.2 cm, which is close to the diameter of the system of 5.6 cm in this study. Therefore, we did not use the TOF information in the reconstruction.

We used the following list mode MLEM update equation:

$$x_j^{n+1} = \frac{x_j^n}{s_j} \sum_{i=1}^{N} P_{k_i,j} \frac{1}{\sum_{l=1}^{M} P_{k_i,l} x_l^n} \tag{1}$$

where x^n is the image after the n-th iteration, $j \in \{1,\ldots, M\}$ is the voxel index, $P_{k_i,j}$ is the probability of detecting an event from voxel j by line of response (LOR) k_i, k_i is the LOR index of the i-th event, N is the total number of events, and s is the sensitivity image shown in figure 5 (s_j is the overall sensitivity of detecting an event from voxel j by all LORs). The system matrix $P_{k_i,j}$ was calculated on-the-fly as detailed in [16, 17].

3. Results

3.1 Reconstructed images

Figure 6 shows the reconstructed images for the mid-axial transverse slice for all the simulation and experimental studies. No smoothing filter was used on the reconstructed images. Visual inspection of the images of the three simulation setups reveals that the “full-ring” and “7.5° angular step” cases give almost equally good images with all the rods clearly resolved; for the images with the “30° angular step” setting, even though all the rods are resolved, the shapes of the rods are deformed, especially for the 0.8 mm diameter rods. One reason for its relatively poorer image quality is that the LOR sampling for the “30° angular step” has missing data for radially off-center positions and the amount of missing data increases with radial distance.

For the experimental result, all the rods except for the 0.8 mm ones (i.e., 1.8, 1.4, and 1.0 mm diameter rods) are resolved at 160 iterations. There are several reasons for the image quality being degraded in the experiment: first, the filling of the FDG in the 0.8 mm hollow channels of the Derenzo phantom was not perfect compared with the simulated source; second, the scattering events caused by the phantom body increased the background noise; third, the random events increased the background noise; fourth, for the layered monolithic crystals, the virtual pixels in the corner and edge regions were slightly larger than 1 mm^2, thus the intrinsic detector resolution in those regions were worse than that in the simulation; fifth, the alignment of the two detector modules in the experiment was not as perfect as in the simulation; sixth, the experiment had additional positioning uncertainty from positron range and non-collinearity which was not modeled in the simulation since back-to-back 511-keV gamma ray pair were used; seventh, the uncertainty introduced by the rotary stage caused image blurring as well. All the above factors contribute to the fact that the 0.8 mm diameter rods were not resolved and the peak to valley ratios were poorer in experiment compared to the similar simulation setup.

Author Manuscript Author Manuscript Author Manuscript Author Manuscript

3.2 Relative recovery coefficient

In [18], the recovery coefficient (RC) is defined as the ratio of the "measured peak activity concentration" to the "true activity concentration". In this study, we did not measure the true activity concentration, thus we were not able to calculate the conventional RC. Instead, we defined a relative recovery coefficient (RRC) as following:

$$\text{Relative Recovery Coefficient} = \frac{\text{Peak activity concentration}}{\text{Peak activity concentration for 1.8 mm rods at 160 iterations}} \tag{2}$$

in which, the denominator was the peak activity concentration for the 1.8 mm rods at 160 iterations for each study respectively. The denominator was the average of the peak values for the three 1.8 mm rods on the fifth column in Figure 6. The numerator is the average of the peak values for each group of same diameter rods at certain iteration numbers.

Figure 7 shows that the RRC saturates as the iteration number increases for all the rods in all four studies. In Figure 8, we compare the RRC values of different diameter rods for all four studies at iteration 160. The three simulation studies give very similar results: as the rod diameter decreases, the RRC value decreases, which is caused by the partial volume effect. The experimental results in Figure 8 have relatively smaller RRC values than the simulation results for rods with 1.0, and 1.4 mm diameters. One reason for the discrepancy between the simulation and experiment is that the detectors used in the experiment have worse spatial resolution than those in simulations, thus the partial volume effect affects the RRC values more in the experiment. In Figure 7 and 8, the RRC for the 0.8 mm rods in experiment was not evaluated as they could not be resolved in the reconstructed images.

3.3 Peak to valley ratio

The peak to valley ratio (P/V) is defined as:

$$\text{Peak to valley ratio} = \frac{\text{Averaged peak value}}{\text{Averaged valley value}} \tag{3}$$

in which the peak values are the maximum pixel density on the rods, and the valley values are the minimum pixel density between the rods for each of the four segments of the phantom. Notice, there were several peaks and valleys in each segment. For example, in the 1.8 mm rod segment, there were three peaks in a triangular arrangement and three valleys between these peaks, which were averaged respectively before the calculation of the peak to valley ratio for this region. For all the subfigures in Figure 9, we notice that as the iteration number increases, the increase rate of P/V ratio decreases, and for some cases, the P/V ratio has approached a saturation value.

Comparing the four subfigures in Figure 9, the P/V ratios for the three simulation studies are all greater than the corresponding experimental values. This result agrees with the observations in Figure 6, in which there are more events in the valley region in experiment. Comparing Figure 9 (a) and (b), the full ring system gives better P/V ratio than the 30° angular step 2-module system. Comparing Figure 9 (b) and (c), we notice a clear advantage of using smaller stepping angle in the 2-module system. Figure 10 compares the P/V ratio

Author Manuscript Author Manuscript Author Manuscript Author Manuscript

for all rod sizes in the four studies when iteration number reaches 160, the 7.5° angular step 2-module system gives better P/V ratios than 30° angular step 2-module system for all rods. Moreover, the 7.5° angular step 2-module system gives better P/V ratios than the full ring system for rods with smaller diameters: 0.8 mm, 1.0 mm, 1.4 mm. One reason is that the LOR sampling is higher in the 7.5° angular step 2-module system than that in the full ring system, which helps resolving smaller structures. Since the simulations for the 2-module system with different stepping angles used the same amount of total acquisition time and generated the same amount of total true events, the result of P/V value for these two simulations in Figure 10 shows clear benefit of using smaller stepping angles when rotating the 2-module system. Thus, we used the 7.5° angular step in the experiment. For the experimental results in Figure 10, the peak to valley ratios with 160 iterations for the 1.0 mm and 0.8 mm rods were 1.53 and 1.14 respectively. Using the Rayleigh criterion of separating two peaks, which is having a peak to valley ratio of 1.23 [19], the 1.0 mm rods were resolved, but the 0.8 mm rods were not.

3.4 Effect of scattered events on image quality

To further study possible factors causing the discrepancy between simulation and experimental results, we conducted one more set of phantom simulations in the full ring scanner configuration. The phantom was the hot rods phantom embedded in a cylinder of 36.0 mm in diameter and 11.2 mm in thickness, which had the same dimensions and material as in the experiment (Figure 4b). The phantom introduced scattered events in the simulation, thus degrading the image quality. Figure 11 shows that the scattered events introduced by the phantom lowers the peak to value ratios for all rod sizes, and therefore is one of the contributing factors for the lower peak to value ratio in the experimental data as shown in Figure 9. In Figure 11, it is shown that the scattered events affect the P/V ratio for bigger rods (1.8 and 1.4 mm) more than for the smaller rods (1.0, 0.8 mm). The reason is that the valley values for smaller rods are already very big due to partial volume effect, the percentage changes for the valley values due to scattered events are much smaller compared with the case for the bigger rods. Several other factors will also degrade the spatial resolution, and therefore the peak to valley ratio, such as the positron range, and non-collinearity of annihilation radiation.

4. Discussion and Conclusion

In this paper, we performed a tomographic study using the layer structure detector modules both in simulation and in experiment. Using GATE simulation, three system geometries were modeled: the 2-module system with large angular step (i.e., 30°), the 2-module system with small angular step (i.e., 7.5°), and the full-ring system. We collected the same number of true coincidence events for the three studies, thus the differences among the reconstructed images in these studies were only caused by the differences of the system geometries and acquisition protocols. Comparing the results of the two 2-module systems, the Derenzo images reconstructed using data collected with small angular step produced better images (visual inspection of the rod shapes) and gave better P/V ratios than those with big angular step. The result agrees with previous studies [17, 20, 21] that higher LOR sampling resulted in more uniform spatial resolution in the reconstructed images, thus better image quality.

Author Manuscript Author Manuscript Author Manuscript Author Manuscript

Comparing the results of the full-ring system with the 2-module system with small angular step, these two systems generated similar images visually as shown in Figure 6. The RRC values in Figure 8 and P/V ratios in Figure 10 also showed similar results for these two studies. Even though the full-ring system gave slightly better P/V ratio for 1.8 mm diameter rods, for smaller rods, the 2-module system with small angular step produced slightly better P/V ratio due to its higher LOR sampling rate. However, for similar image quality, compared to 2,688-second acquisition time for the 2-module system, the acquisition time for the full-ring system was only 380 seconds due to its larger solid angle coverage.

For the experiments, we built a 2-module system with the Compton PET detectors. We virtually binned the layer structure monolithic crystals into 1 mm^2 cells, except for the edge and corner regions where the virtual pixels were slightly larger. Compared with the phantom used in simulation, which had back-to-back annihilation photons with no attenuating/scattering medium modeled, a 3D printed phantom was used to contain the radioactive FDG solution in the experiment, which introduced image degrading factors such as positron range, non-collinearity, attenuation and scatter. The same algorithm used in simulation studies was used for the experimental data to reconstruct images in Figure 6. For the experimental results, except for the 0.8 mm diameter rods, all other three sized rods were clearly resolved. Figure 8 and Figure 10 indicated that the RRC and P/V ratio for the experimental results were worse than all the three simulation results, which can be explained by the imperfection of the detectors and phantoms used in the experiment, and the inclusion of scatter and random events in the experiment data. Future studies will include improvement of the experimental hardware, and attenuation/random/scatter corrections in the reconstruction process for the experimental data.

In conclusion, the results of this work have demonstrated that the layer structure Compton PET module can be used as the foundation to build a high spatial resolution PET scanner, which can resolve fine structure image as small as 1 mm. At the same time, since this module also has high energy/timing resolution, and the thickness of the module can be increased without degrading these parameters. A full ring scanner built with Compton PET modules will have high performance in terms of all key metrics for a PET scanner.

Acknowledgments

The authors would like to thank members of the MIPET group at UC Davis for helpful discussions. This work was funded by NIH R01 EB019439, R01 EB028337 and R01 EB000194.

References

[1]. Phelps ME, PET: Molecular Imaging and Its Biological Applications, New York: Springer, 2004.

[2]. Badawi RD, Shi H, Hu P, Chen S, Xu T, Price PM, Ding Y, Spencer BA, Nardo L, Liu W, Bao J, Jones T, Li H, and Cherry SR, “First Human Imaging Studies with the EXPLORER Total-Body PET Scanner,” J Nucl Med, vol. 60, no. 3, pp. 299–303, 03, 2019. [PubMed: 30733314]

[3]. Levin CS, “Design of a high-resolution and high-sensitivity scintillation crystal array for PET with nearly complete light collection,” IEEE Tran. Nucl. Sci, vol. 49, no. 5, pp. 2236–2243, 2002.

[4]. Lewellen T, “The Challenge of Detector Designs for PET,” AJR Am J Roentgenol, vol. 195, no. 2, pp. 301–309, 2010. [PubMed: 20651184]

Author Manuscript Author Manuscript Author Manuscript Author Manuscript

[5]. Seifert S, van der Lei G, van Dam HT, and Schaart DR, “First characterization of a digital SiPM based time-of-flight PET detector with 1 mm spatial resolution,” Phys. Med. Biol, vol. 58, no. 9, pp. 3061–3074, 2013. [PubMed: 23587636]

[6]. Pierce LA, Pedemonte S, DeWitt D, MacDonald L, Hunter WCJ, Van Leemput K, and Miyaoka R, “Characterization of highly multiplexed monolithic PET / gamma camera detector modules,” Phys. Med. Biol, vol. 63, no. 7, pp. 16, 2018.

[7]. Li X, and Furenlid LR, “An analysis of side readouts of monolithic scintillation crystals,” Proc. of SPIE, vol. 9969, pp. 996908, 2016.

[8]. Li X, Ruiz-Gonzalez M, and Furenlid LR, “An edge-readout, multilayer detector for positron emission tomography,” Med. Phys, vol. 45, no. 6, pp. 2425–2438, 2018. [PubMed: 29635734]

[9]. Peng P, Judenhofer M, Jones A, and Cherry S, “Compton PET: a simulation study for a PET module with novel geometry and machine learning for position decoding,” Biomed. Phys. Eng. Express, vol. 5, pp. 015018, 2019. [PubMed: 34290885]

[10]. Tao L, Li X, Furenlid LR, and Levin CS, “Deep learning based methods for gamma ray interaction location estimation in monolithic scintillation crystal detectors,” Phys Med Biol, vol. 65, no. 11, pp. 115007, 06, 2020. [PubMed: 32235062]

[11]. Barrio J, Neus Cucarella N, Gonzalez AJ, Freire M, Ilisie V, and Benlloch JM, “Characterization of a High-Aspect Ratio Detector With Lateral Sides Readout for Compton PET,” IEEE Transactions on Radiation and Plasma Medical Sciences, vol. 4, no. 5, pp. 546–554, 2020.

[12]. Peng P, Judenhofer MS, and Cherry SR, “Compton PET: a layered structure PET detector with high performance,” Phys Med Biol, vol. 64, no. 10, pp. 10LT01, 05, 2019.

[13]. Zhang X, Cherry SR, Xie Z, Shi H, Badawi RD, and Qi J, “Subsecond total-body imaging using ultrasensitive positron emission tomography,” Proc Natl Acad Sci U S A, 1, 2020.

[14]. Jan S, Santin G, Strul D, Staelens S, Assie K, Autret D, Avner S, Barbier R, Bardies M, Bloomfield PM, Brasse D, Breton V, Bruyndonckx P, Buvat I, Chatziioannou AF, Choi Y, Chung YH, Comtat C, Donnarieix D, Ferrer L, Glick SJ, Groiselle CJ, Guez D, Honore PF, Kerhoas-Cavata S, Kirov AS, Kohli V, Koole M, Krieguer M, van der Laan DJ, Lamare F, Largeron G, Lartizien C, Lazaro D, Maas MC, Maigne L, Mayet F, Melot F, Merheb C, Pennacchio E, Perez J, Pietrzyk U, Rannou FR, Rey M, Schaart DR, Schmidtlein CR, Simon L, Song TY, Vieira JM, Visvikis D, de Walle RV, Wieers E, and Morel C, “GATE: a simulation toolkit for PET and SPECT,” Phys. Med. Biol, vol. 49, no. 19, pp. 4543–4561, 10, 2004. [PubMed: 15552416]

[15]. Levitan E, and Herman GT, “A maximum a posteriori probability expectation maximization algorithm for image reconstruction in emission tomography,” IEEE Trans Med Imaging, vol. 6, no. 3, pp. 185–92, 1987. [PubMed: 18244020]

[16]. Huesman RH, Klein GJ, Moses WW, Qi JY, Reutter BW, and Virador PRG, “List-mode maximum-likelihood reconstruction applied to positron emission mammography (PEM) with irregular sampling,” IEEE Trans. Med. Imag, vol. 19, no. 5, pp. 532–537, 5, 2000.

[17]. Zhang X, Stortz G, Sossi V, Thompson CJ, Retière F, Kozlowski P, Thiessen JD, and Goertzen AL, “Development and evaluation of a LOR-based image reconstruction with 3D system response modeling for a PET insert with dual-layer offset crystal design,” Phys Med Biol, vol. 58, no. 23, pp. 8379–99, 12, 2013. [PubMed: 24217067]

[18]. Phelps ME, Cherry SR, and Dahlbom M, PET: Physics, Instrumentation, and ScannersNew York: Springer, 2006.

[19]. Comesana DF, Holland KR, and Fernandez Grande E, “Spatial resolution limits for the localization of noise sources using direct sound mapping,” Journal of Sound and Vibration, no. 375, pp. 53–62, 2016.

[20]. Suk JY, Thompson CJ, Labuda A, and Goertzen AL, “Improvement of the spatial resolution of the MicroPET R4 scanner by wobbling the bed,” Med Phys, vol. 35, no. 4, pp. 1223–31, 4, 2008. [PubMed: 18491514]

[21]. Metzler SD, Matej S, and Karp JS, “Resolution Enhancement in PET Reconstruction Using Collimation,” IEEE Trans Nucl Sci, vol. 60, no. 1, pp. 65–75, 2, 2013. [PubMed: 23493920]

Author Manuscript

Author Manuscript

Author Manuscript

Author Manuscript

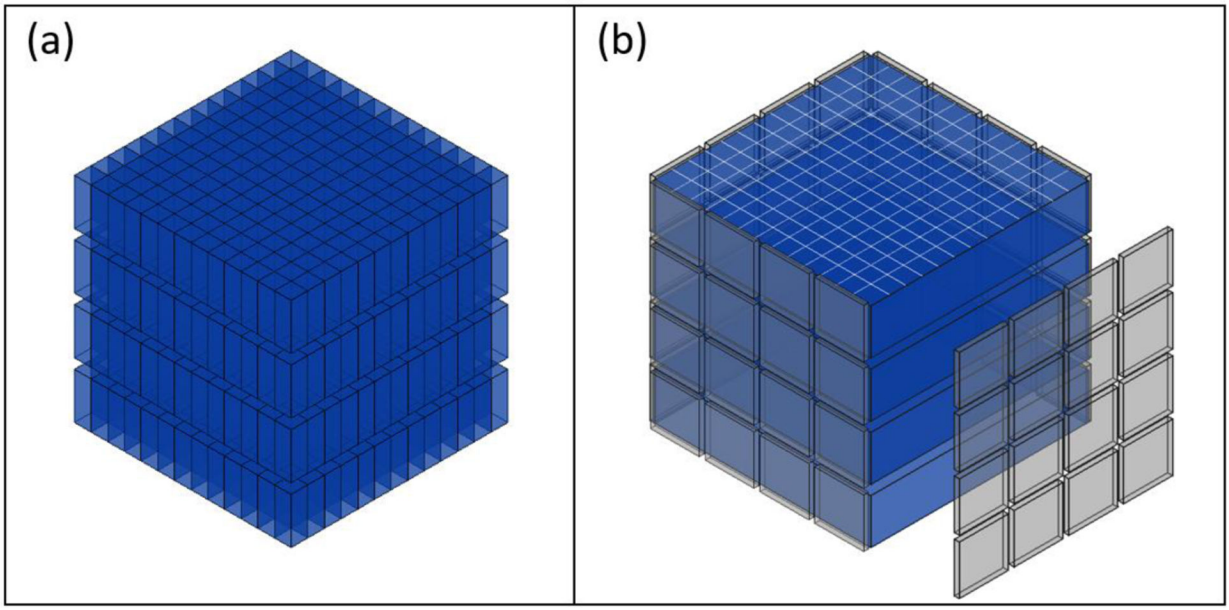

Figure 1.
Schematics for detector module used in (a) GATE simulation and (b) experiment.

Author Manuscript

Author Manuscript

Author Manuscript

Author Manuscript

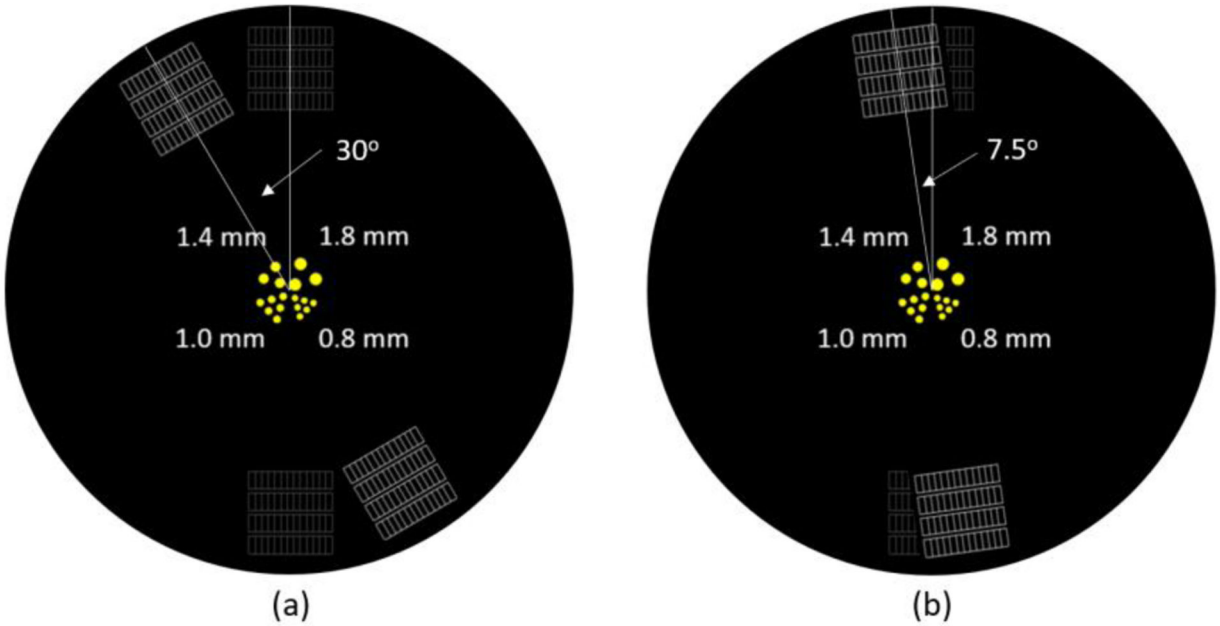

Figure 2.

View of the scanner along the axial direction. The two schematics show simulations with two angular steps of (a) 30° and (b) 7.5°.

Author Manuscript

Author Manuscript

Author Manuscript

Author Manuscript

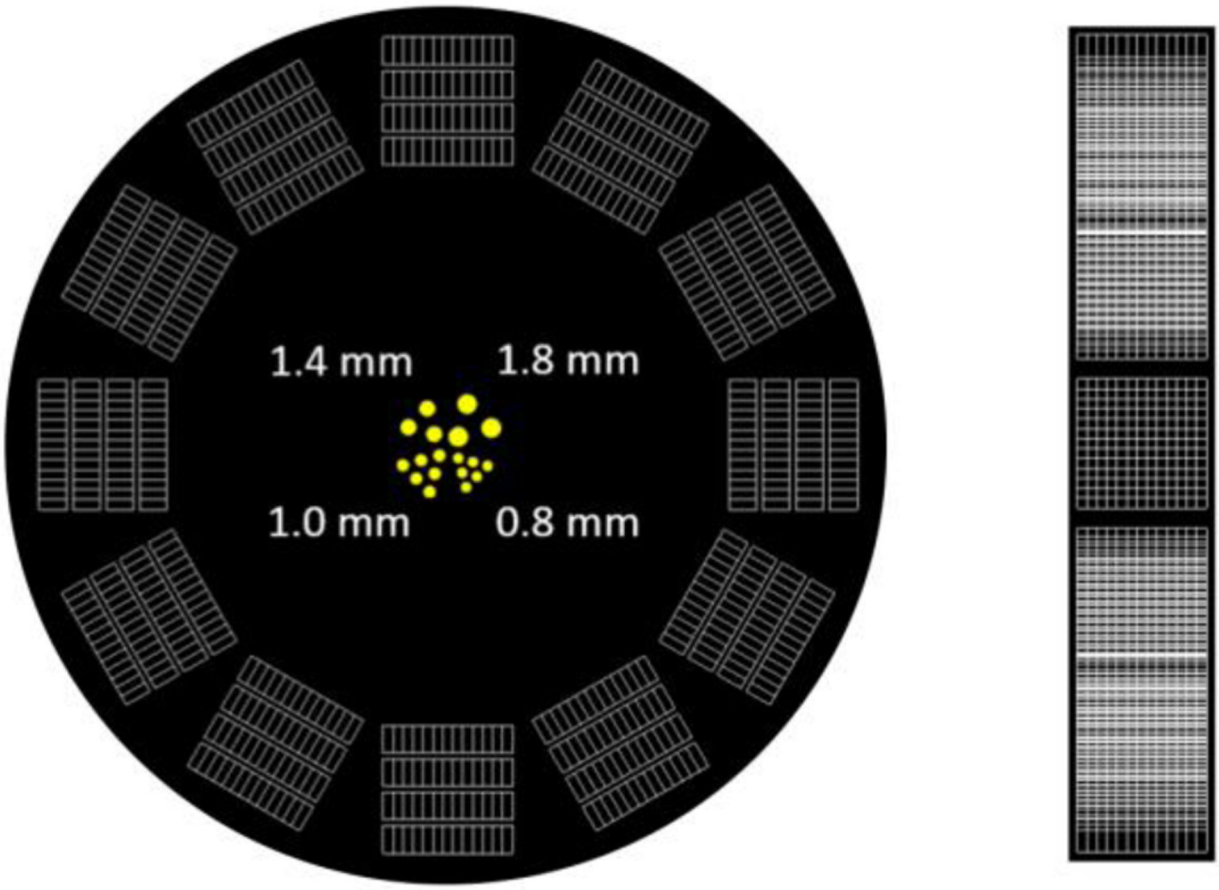

Figure 3.

Views of the scanner along the axial (left) and radial (right) directions. Note, the gantry diameter is 56 mm.

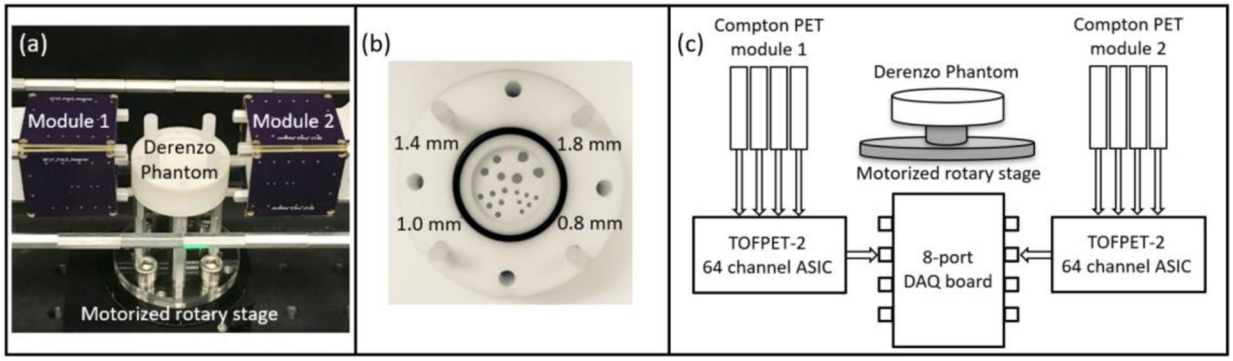

Figure 4.

(a): A photograph of the experimental setup. (b): A photograph of the customized Derenzo phantom. (c): A schematic plot showing the experimental setup and the data stream from the detector modules to the data acquistion system.

Author Manuscript Author Manuscript Author Manuscript Author Manuscript

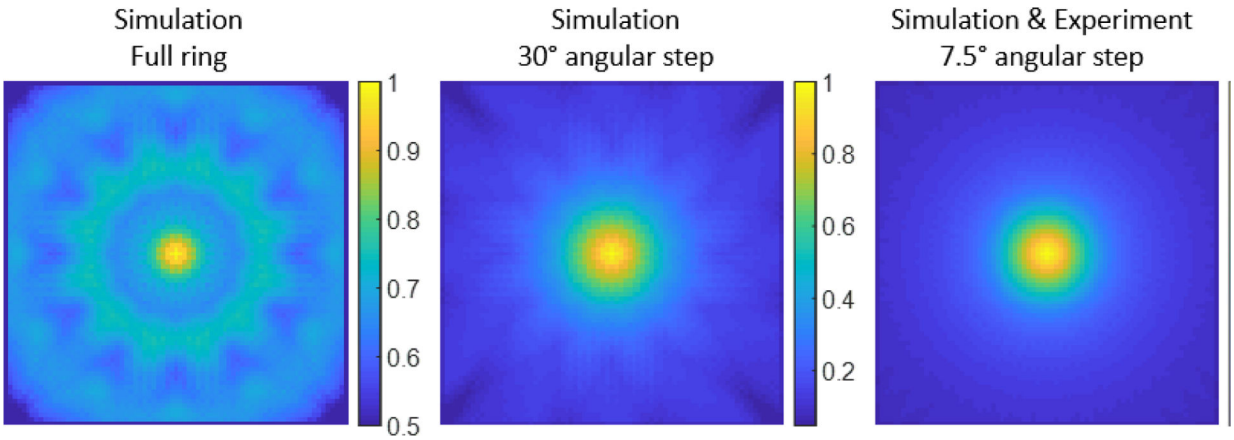

Figure 5.

Calculated sensitivity map. Left: simulation with the full-ring scanner; middle: simulation with the 2-module scanner with 30° angular step; right: simulaton and experiment with the 2-module scanner with 7.5° angular step.

Author Manuscript
Author Manuscript
Author Manuscript
Author Manuscript

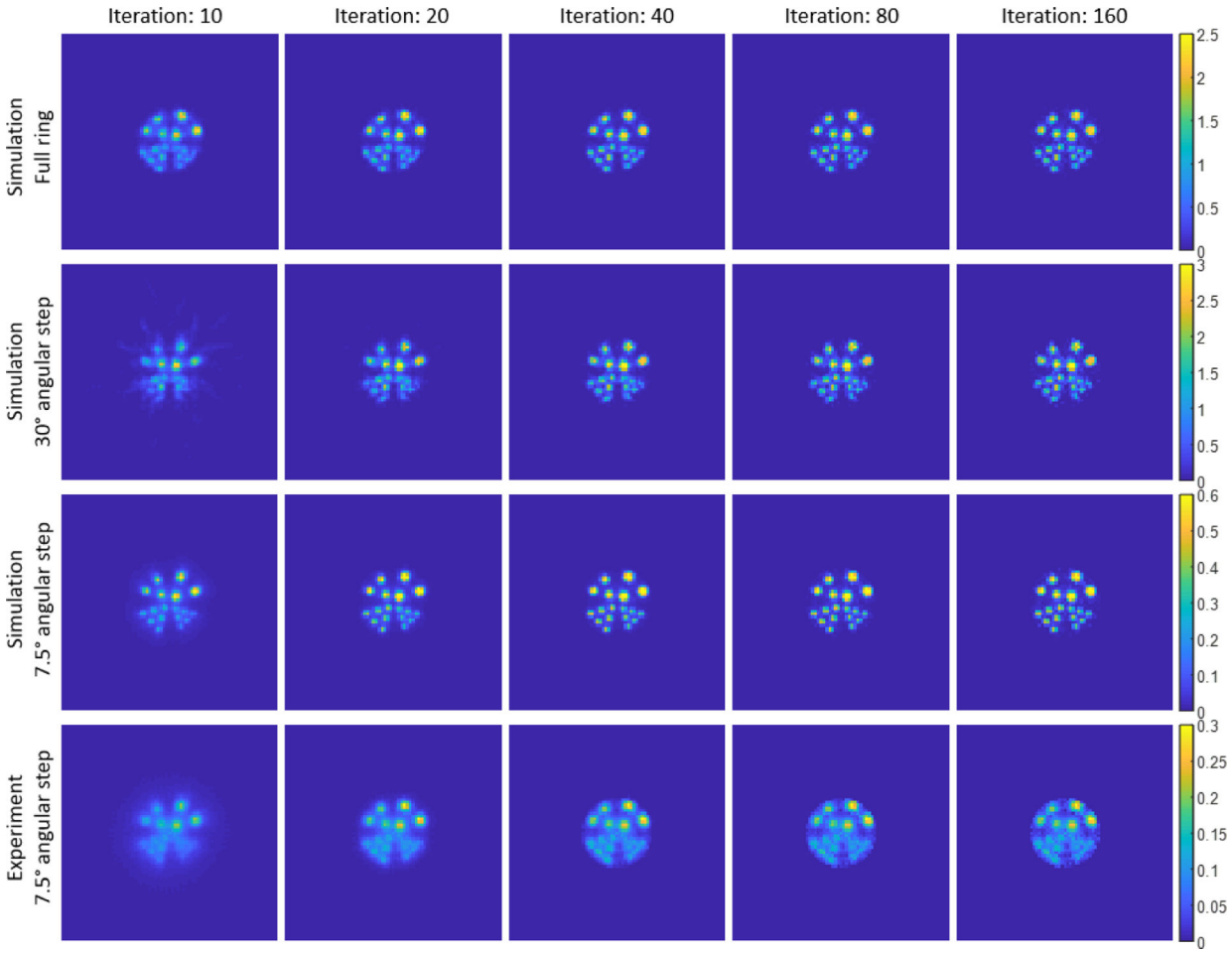

Figure 6.

The reconstructed images for the mid-axial transverse slice for all the simulation and experimental studies: full-ring simulation (1st row), 2-module 30° angular step simulation (2nd row), 2-module 7.5° angular step simulation (3rd row), and 2-module 7.5° angular step experiment (4th row). Different columns are for different number of MLEM iterations.

Author Manuscript Author Manuscript Author Manuscript Author Manuscript

Author Manuscript Author Manuscript Author Manuscript Author Manuscript

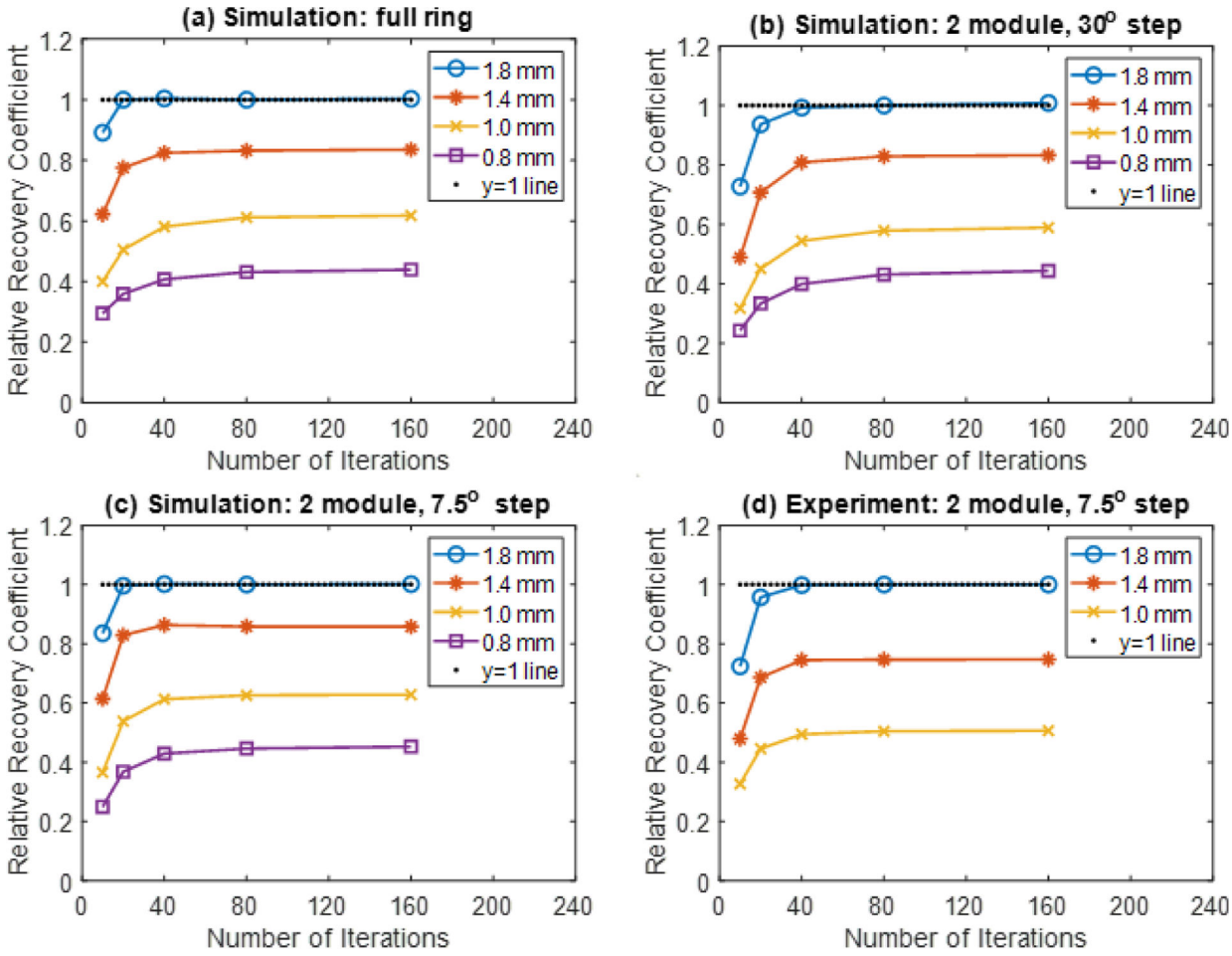

Figure 7.

Relative recovery coefficient for the four studies: (a) full ring simulation, (b) 2-module 30° angular step simulation, (c) 2-module 7.5° angular step simulation, (d) 2-module 7.5° angular step experiment.

Author Manuscript Author Manuscript Author Manuscript Author Manuscript

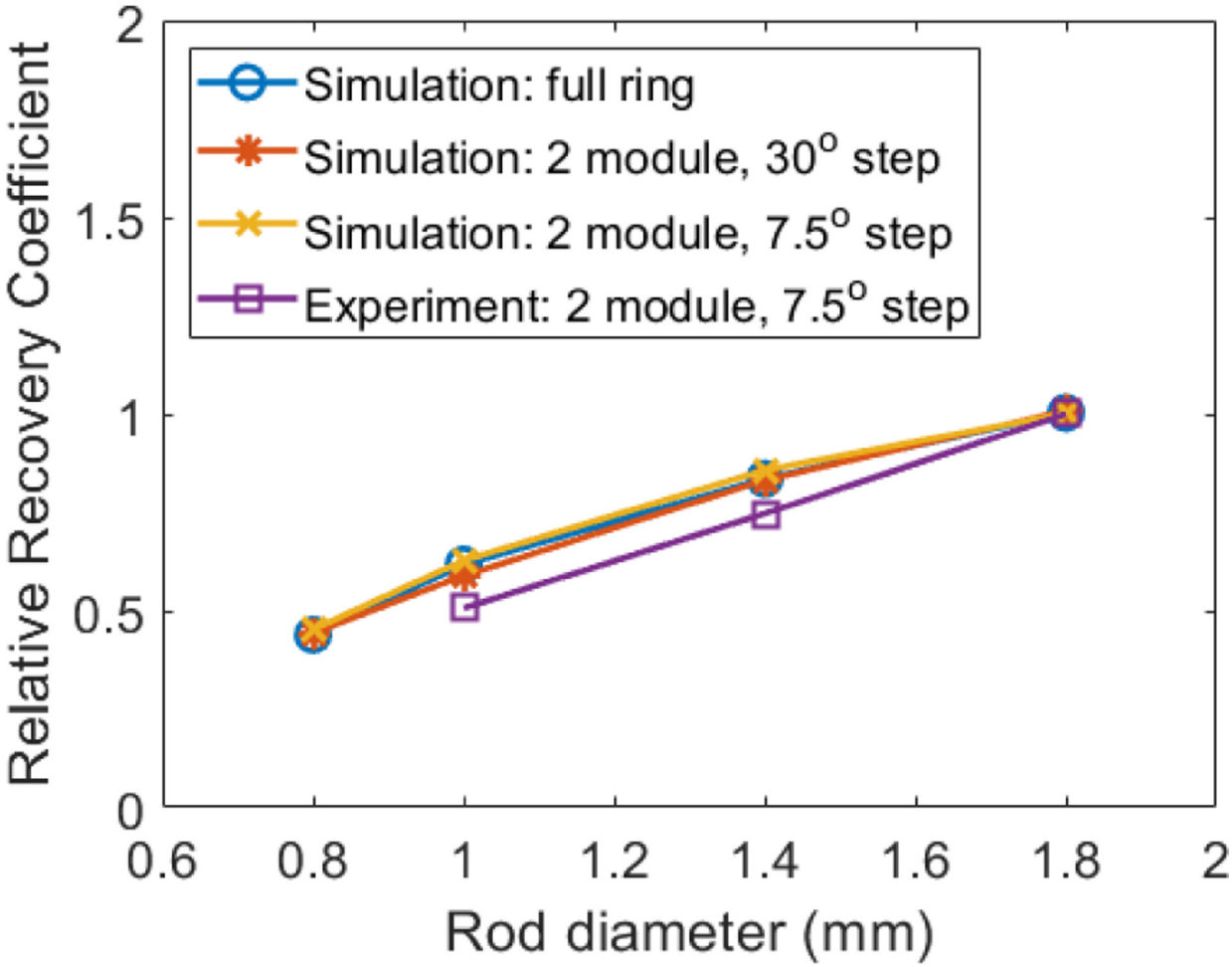

Figure 8.
Relative recovery coefficient for different size rods at iteration 160.

Author Manuscript Author Manuscript Author Manuscript Author Manuscript

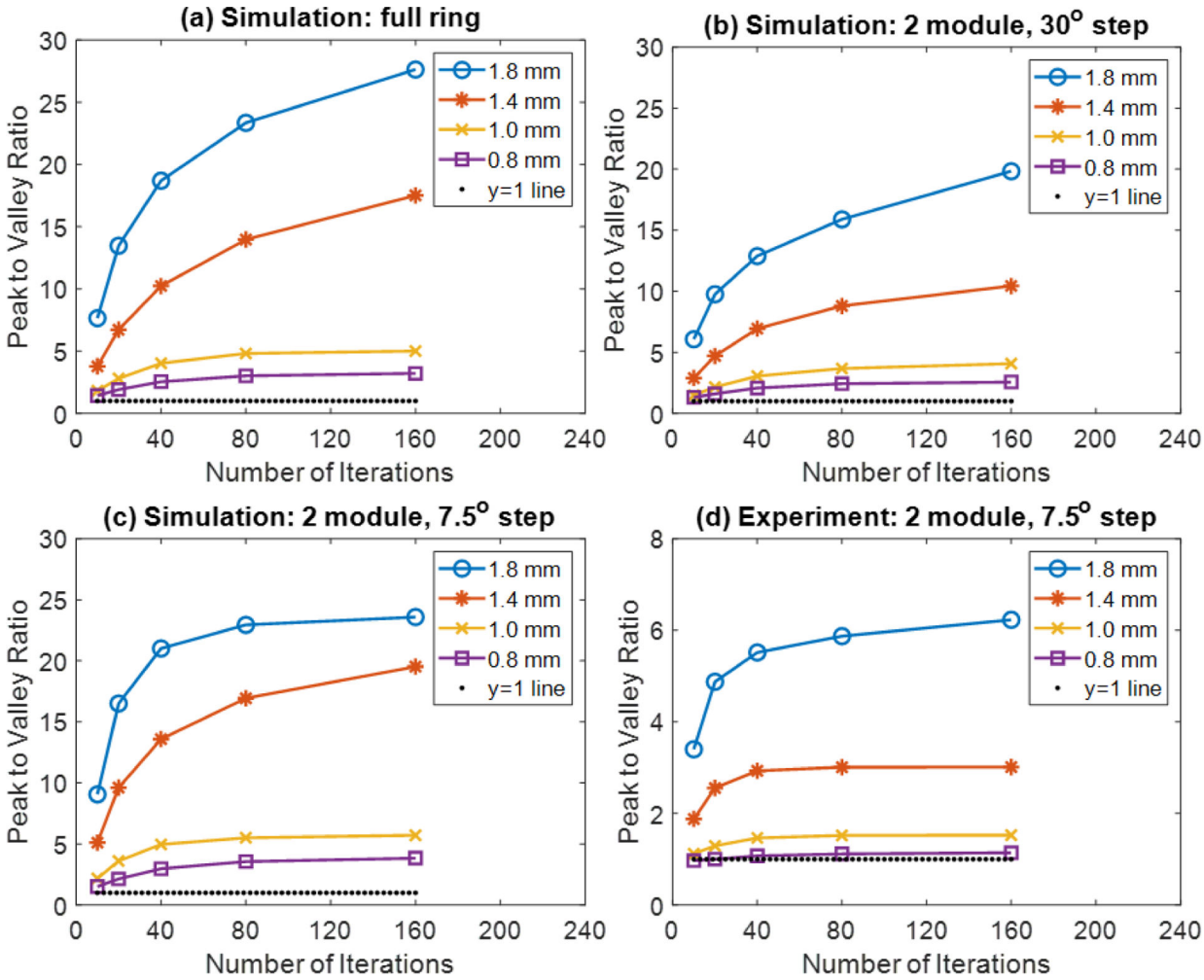

Figure 9.

Peak to valley ratio for the four studies: (a) full-ring simulation, (b) 2-module 30° angular step simulation, (c) 2-module 7.5° angular step simulation, (d) 2-module 7.5° angular step angle experiment.

Author Manuscript Author Manuscript Author Manuscript Author Manuscript

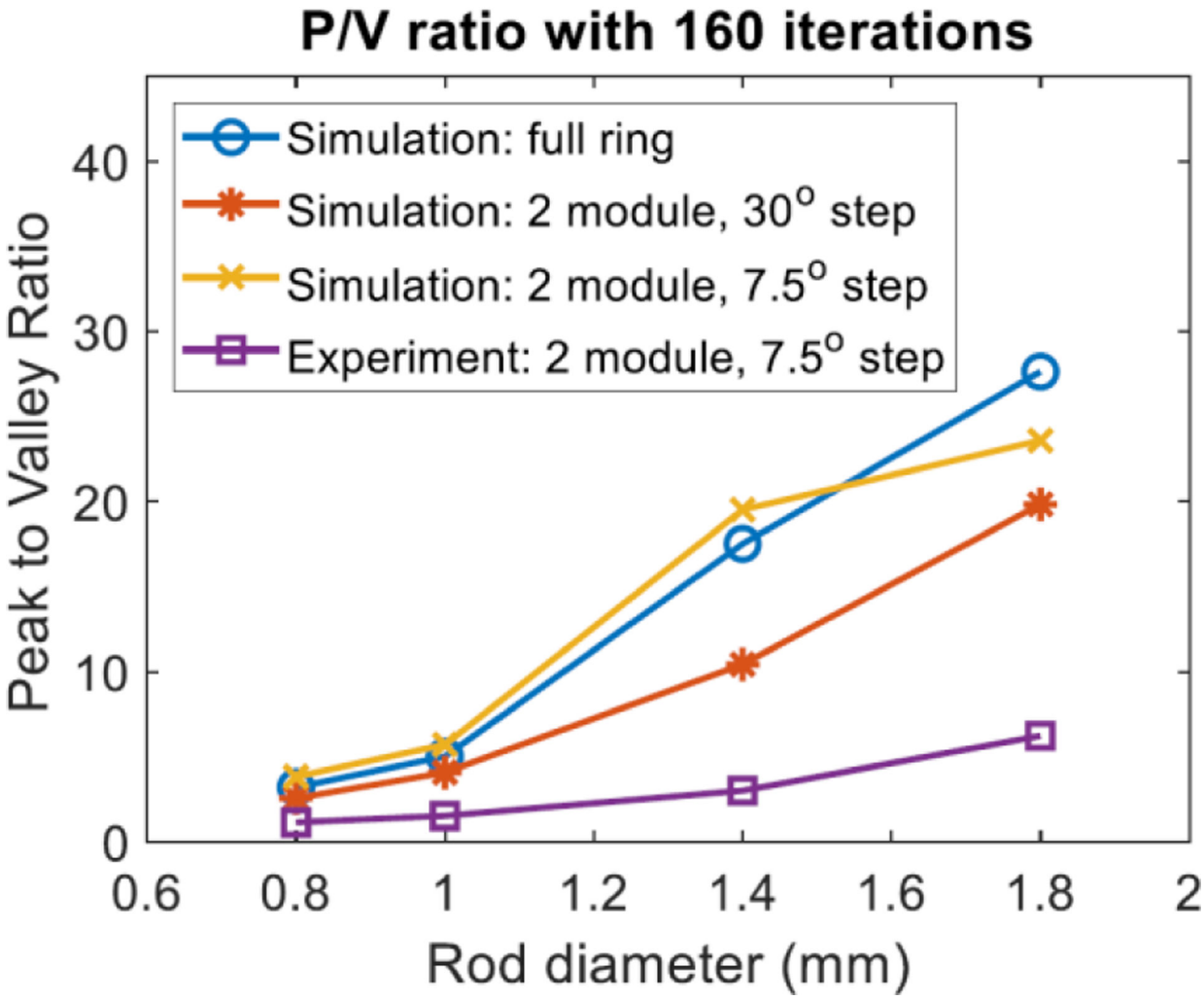

Figure 10.
Peak to valley ratio for different size rods when iteration number reaches 160.

Author Manuscript Author Manuscript Author Manuscript Author Manuscript

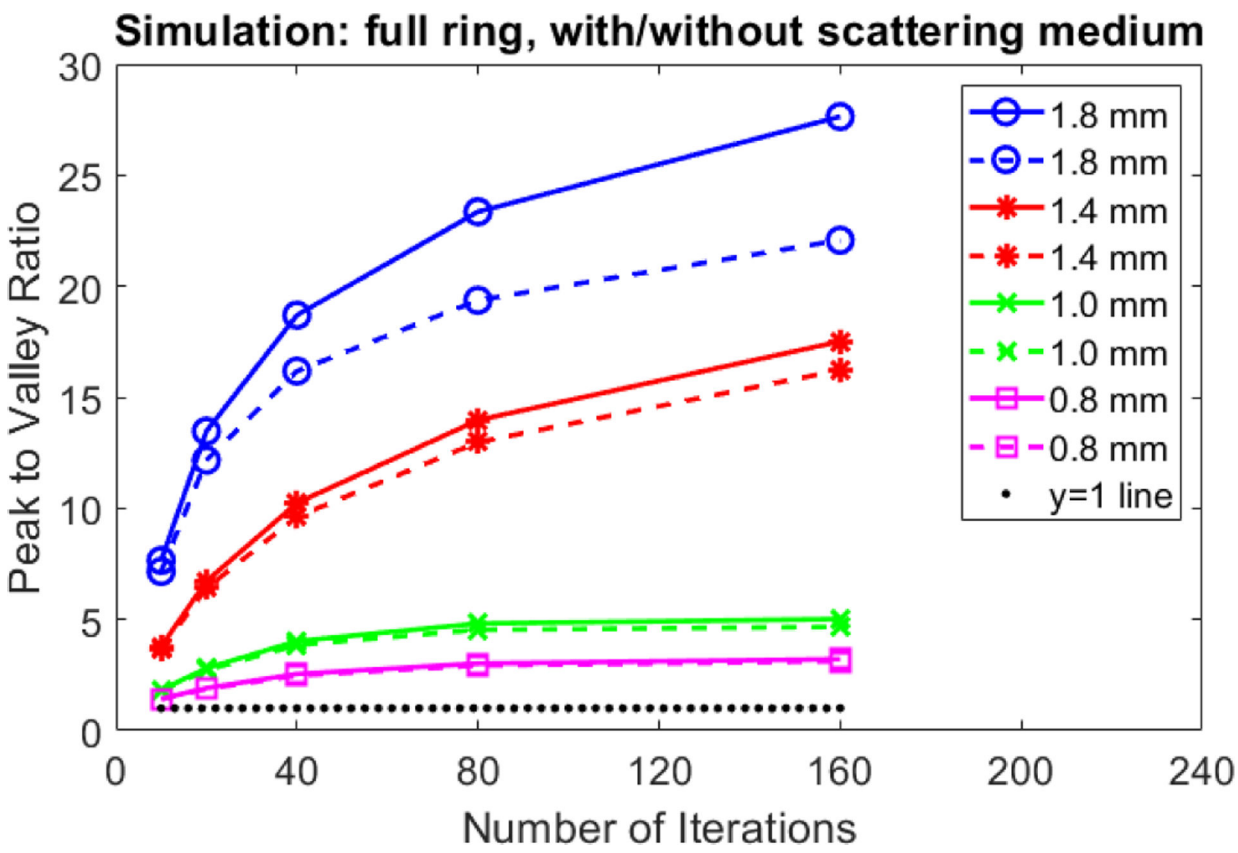

Figure 11.
Peak to valley ratios for the full ring simulation with (dashed line) and without (solid line) scattering medium.